A multiscale and multiphysics numerical framework for modelling of hygrothermal ageing in laminated composites

Rocha, I. B C M; van der Meer, F. P.; Nijssen, R. P L; Sluys, L. J.

DOI
10.1002/nme.5542

Publication date
2017

Document Version
Accepted author manuscript

Published in
International Journal for Numerical Methods in Engineering

This is an Accepted Manuscript of an article published by Wiley in:
International Journal for Numerical Methods in Engineering
First published: 17 March 2017,
available online: http://dx.doi.org/10.1002/nme.5542

A multiscale and multiphysics numerical framework for modelling of hygrothermal ageing in laminated composites

I. B. C. M. Rocha[1,2], F. P. van der Meer[2], R. P. L. Nijssen[1], and L. J. Sluys[2]

[1]Knowledge Centre WMC, Kluisgat 5, 1771MV Wieringerwerf, The Netherlands
[2]Delft University of Technology, Faculty of Civil Engineering and Geosciences, P.O. Box 5048, 2600GA Delft, The Netherlands

Abstract

In this work, a numerical framework for modelling of hygrothermal ageing in laminated composites is proposed. The model consists of a macroscopic diffusion analysis based on Fick's second law coupled with a multiscale FE^2 stress analysis in order to take microscopic degradation mechanisms into account. Macroscopic material points are modelled with a representative volume element (RVE) with random fibre distribution. The resin is modelled as elasto-plastic with damage and cohesive elements are included at the fibre/matrix interfaces. The model formulations and the calibration of the epoxy model using experimental results are presented in detail. A study into the RVE size is conducted and the framework is demonstrated by simulating the ageing process of a unidirectional specimen immersed in water. The influence of transient swelling stresses on microscopic failure is investigated and failure envelopes of dry and saturated micromodels are compared.
Keywords: Composites, Multiscale, Damage, Micromechanics

1 Introduction

Research on composite material usage optimization has been on the rise in the past few years, and particular focus is being given to reducing design uncertainty. In the case of wind turbine blade design, large rotor diameters are necessary in order to increase power output but they also bring significant increases in gravity bending fatigue loads. The reduction of design uncertainty through a better understanding of material behaviour and its interaction with service environment becomes a promising approach.

Wind turbines are subjected to extreme environmental conditions during service life, including exposure to moisture, high/low temperatures, UV radiation, sand and water droplet erosion. For the composite materials that comprise the main load bearing structure of a blade, the combined influence of temperature and moisture ingression is regarded as the most critical environmental effect [1]. Water ingress occurs through a diffusion process dependent on the temperature and the concentration of water molecules in the surrounding environment.

Once absorbed, water molecules become attached to polymer chains, promoting plasticization (lower modulus and strength) and swelling [2, 3]. Depending on the polymer system, chains may also be broken through hydrolytic reactions [4]. Since most fibre systems used in industrial applications (*e.g.* glass, carbon) do not absorb water and therefore do not swell, differential swelling stresses arise [3]. Water molecules also weaken the interface adhesion between fibres and resin, facilitating debonding [5, 6]. These degradation mechanisms may act at different time scales and be either reversible or irreversible upon drying, increasing the complexity of the problem at hand. The combination of such effects makes a purely experimental characterisation of the hygrothermal ageing phenomenon a difficult task.

A number of authors has therefore advocated numerical modelling in order to simulate the hygrothermal ageing process in polymers and composites [3, 2, 7, 8] as well as in porous materials [9]. Since the mentioned degradation effects act on the microsopic material constituents, a micromechanics approach becomes a necessity. However, it is also important to predict how such microscopic processes affect macroscopic material behaviour. Naya *et al.* [7] successfully used micromechanics to predict the wet properties of a unidirectional ply by fitting a mesoscale failure criterion, although the swelling phenomenon was not considered. Such a numerical homogenisation approach entails a one-way upscaling procedure after which the microscopically obtained failure envelope can be used in mesolevel analysis.

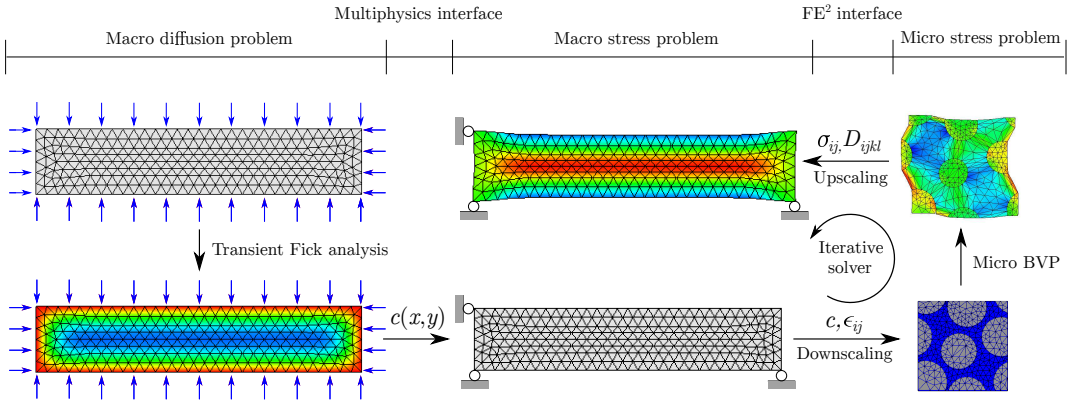

Figure 1: Schematic representation of the multiphysics/multiscale model for hygrothermal ageing

However, macroscopic phenomena such as transient swelling stresses during diffusion [10] may also influence the resultant microscopic degradation processes. Joliff *et al.* [3] simulated the immersion of a macroscopic specimen including diffusion and differential swelling by explicitly meshing its complete microstructure. The authors demonstrated the importance of including differential swelling in the ageing model, although material failure and degradation (plasticization, interface weakening) were not included. However, such a direct numerical simulation (DNS) approach becomes computationally infeasible if an iterative failure analysis is performed at the same time.

In order to simultaneously account for macroscopic transient phenomena and microscopic failure mechanisms, a concurrent multiscale approach can be chosen by solving finite element problems at both macro and micro scales and coupling them through homogenisation by means of a so-called FE^2 approach [11]. A large body of literature is dedicated to the treatment of pure stress analysis in FE^2 [12, 13], including consistent treatment of material failure across scales [14] and modelling of processes at different time scales [15, 16]. On the other hand, treatment of other field problems such as heat transfer [17], mass diffusion [18] and coupled diffusion-reaction [19] in an FE^2 framework is still not extensively documented. Particularly for multiphysics applications, in which multiple fields are homogenised, no consensus exists on how to couple the physical processes at play (full [20] or one-way coupling [21]) or how to perform macro to micro transitions of non-mechanical fields (constant [18] or periodically fluctuating microscopic fields [21]). To the best of the authors' knowledge, a framework that best suits the particular problem of hygrothermal ageing in laminated composites has not been previously treated.

In this work, a multiphysics and multiscale framework is proposed for modelling hygrothermal ageing in composites. A diffusion model at the macroscale is coupled with an FE^2 homogenisation scheme in order to model swelling and material degradation at both the micro- and macroscales. At the microscale, failure is modelled in a representative volume element (RVE) of the material by using an elasto-plastic epoxy model with damage [22] combined with cohesive interfaces around every fibre [23]. A model for concentration-dependent mechanical properties with a single degradation factor is proposed. At every time step, the spatial scales are coupled by passing the local strain and water concentration to micromodels embedded at every material point, from which stress and tangent stiffness are in turn obtained. The model formulations and the calibration of the epoxy model using experimental results are shown in detail. A study on the required RVE size is performed and the framework is demonstrated by modelling ageing in a unidirectional short-beam shear test specimen immersed in water.

2 Model formulation

2.1 Mathematical notation

In this work, both index notation and matrix notation will be used to represent tensors and vectors. When index notation is used, the indices i, j, k, l range from one to the number of spatial dimensions of the problem being solved. In products between two entities in index notation, summation over repeated indices is implied. In matrix notation, vectors are represented by boldfaced lower-case symbols while matrices are given by boldfaced upper-case symbols. When representing stresses and strains in matrix notation, the use of Voigt notation is implied.

As the formulations presented here span multiple spatial scales, the superscripts M and m will be used

to represent macroscopic and microscopic entities, respectively. For the sake of generality, all formulations will be presented considering three-dimensional macro- and micromodels.

2.2 Macroscale problem

In order to simulate the ageing process at the macroscopic scale, a coupled multiphysics problem is solved involving water diffusion and mechanical stresses (Figure 1). At a given point in time, the water concentration field c^{M} is given by Fick's second law of diffusion:

$$\dot{c}^{\mathrm{M}} + \frac{\partial j_i^{\mathrm{M}}}{\partial x_i^{\mathrm{M}}} = 0 \tag{1}$$

where j_i^{M} are the water flux components, given by:

$$j_i^{\mathrm{M}} = -D_{ij}^{\mathrm{M}} \frac{\partial c}{\partial x_j^{\mathrm{M}}} \tag{2}$$

and D_{ij}^{M} is a diffusivity tensor. The water movement is therefore modelled as a smooth molecular motion driven by concentration gradients.

It is worth mentioning that the water uptake model of Eq. (1) is suitable for resin systems featuring one-phase Fickian diffusion behaviour, which is the case for the epoxy system used to calibrate the present formulations [24] and systems studied by multiple other authors [3, 4, 5, 10]. For systems that display a two-phase behaviour, the model must be expanded into a diffusion-reaction scheme, which entails the inclusion of a reaction term into Eq. (1). Details of such procedure can be found in [25].

An increase in water concentration will cause the macroscopic specimen to swell. If the specimen is constrained or if the concentration field is not constant at every point in space, swelling stresses will be generated. Stress equilibrium is enforced by:

$$\frac{\partial \sigma_{ji}^{\mathrm{M}}}{\partial x_j^{\mathrm{M}}} + b_i = 0 \tag{3}$$

where b_i are body forces. In stress analysis, it is also necessary to define the relationship between the strain and displacement fields. Here, the small strain tensor is used:

$$\epsilon_{ij}^{\mathrm{M}} = \frac{1}{2}\left(\frac{\partial u_i^{\mathrm{M}}}{\partial x_j^{\mathrm{M}}} + \frac{\partial u_j^{\mathrm{M}}}{\partial x_i^{\mathrm{M}}}\right) \tag{4}$$

For the rest of this section, matrix notation will be adopted and the superscript M will be dropped to keep the notation compact. In order to solve the multiphysics problem with the Finite Element Method (FEM), the macroscopic volume Ω is discretised in elements and both concentration and displacement fields are interpolated using the nodal values $\overline{\mathbf{c}}$ and $\overline{\mathbf{u}}$:

$$c = \mathbf{N}_c \overline{\mathbf{c}} \qquad \mathbf{u} = \mathbf{N}_u \overline{\mathbf{u}} \tag{5}$$

where $\mathbf{N}_c$ and $\mathbf{N}_u$ are shape functions for concentration and displacements, respectively.

Substituting the discretized fields of Eq. (5) into Eqs. (1) and (3) and solving them in their weak form, the global moisture and stress equilibrium equations are obtained:

$$\mathbf{K}_c \overline{\mathbf{c}} + \mathbf{C}\dot{\overline{\mathbf{c}}} = \mathbf{f}_{\mathrm{j}} \qquad \mathbf{K}_u \overline{\mathbf{u}} = \mathbf{f}_{\mathrm{ext}} \tag{6}$$

with $\dot{\overline{\mathbf{c}}}$ being the nodal values of the time derivative of the concentration, $\mathbf{K}_c$, $\mathbf{C}$ and $\mathbf{f}_j$ are the diffusion matrix, the water capacity matrix and the external flux vector, respectively, given by:

$$\mathbf{K}_c = \int_\Omega \mathbf{B}_c^{\mathrm{T}} \mathbf{D}_c \mathbf{B}_c d\Omega \qquad \mathbf{C} = \int_\Omega \mathbf{N}_c^{\mathrm{T}} \mathbf{N}_c d\Omega \qquad \mathbf{f}_j = \int_{\Gamma_j} \mathbf{N}_c^{\mathrm{T}} \mathbf{j}_\Gamma d\Gamma \tag{7}$$

and $\mathbf{K}_u$ and $\mathbf{f}_{\mathrm{ext}}$ are the stiffness matrix and the external force vector, respectively:

$$\mathbf{K}_u = \int_\Omega \mathbf{B}_u^{\mathrm{T}} \mathbf{D}_u \mathbf{B}_u d\Omega \qquad \mathbf{f}_{\mathrm{ext}} = \int_\Omega \mathbf{N}_u^{\mathrm{T}} \mathbf{b} d\Omega + \int_{\Gamma_\sigma} \mathbf{N}_u^{\mathrm{T}} \boldsymbol{\sigma}_\Gamma d\Gamma \tag{8}$$

where Γ denotes surfaces with prescribed water flux or stresses and integrals in the macroscopic domain Ω imply element-wise integration followed by an assembly procedure.

In Eqs. (7) and (8), $\mathbf{B}$ contains spatial derivatives of the shape functions and $\mathbf{D}_c$ is the diffusivity tensor of Eq. (2). In this work, the diffusivity is considered independent of the water concentration and is thus constant throughout the analysis. Finally, $\mathbf{D}_u$ is the tangent material stiffness matrix. In contrast with the diffusivity behaviour, a constitutive model for strains is not assumed *a priori* but is instead substituted by embedded micromodels at every integration point. Each micromodel receives the strain from the macromodel and returns the associated stress tensor and tangent stiffness. The down- and upscaling procedures involved in this process are shown in Section 2.4.

As can be seen in Figure 1, a one-way coupling exists between the diffusion and stress models. The diffusion analysis is not affected by the stress state of the material and the interaction between the two problems shown in Eq. (6) does not need to be solved iteratively. Instead, the diffusion model is solved first and the resultant concentration field is passed to the stress model. This type of staggered operator-split strategy was also adopted by other authors [21, 18].

2.3 Microscale problem

The micromodel considered in this work consists in a Representative Volume Element (RVE) of unidirectional fibres surrounded by resin, with interface elements around every fibre, allowing for the modelling of fibre-matrix interface debonding. The difference in length scales between macro- and micromodels is considered large enough for the principle of separation of scales [11] to be applied. Thus, the macroscopic strains and water concentration are considered uniform over the microscopic domain and only the stress equilibrium problem is considered:

$$\frac{\partial \sigma_{ji}^{\mathrm{m}}}{\partial x_j^{\mathrm{m}}} = 0 \qquad \epsilon_{ij}^{\mathrm{m}} = \frac{1}{2}\left(\frac{\partial u_i^{\mathrm{m}}}{\partial x_j^{\mathrm{m}}} + \frac{\partial u_j^{\mathrm{m}}}{\partial x_i^{\mathrm{m}}}\right) \tag{9}$$

where the body forces b_i are neglected. The reasoning behind considering that the water concentration is constant over the entire micro domain is presented in Section 2.4. Solving the problem using FEM involves solving a system of equations similar to the second expression of Eq. (6) but now the integrations are performed over the microscopic volume ω. Additionally, since the micromodel includes interface elements around every fibre, the displacement jumps along them are also interpolated and their contribution to the global stiffness matrix is obtained via:

$$[\![\mathbf{u}]\!] = \mathbf{N}_{[\![\mathrm{u}]\!]}\overline{\mathbf{u}} \quad \Rightarrow \quad \mathbf{K}_{[\![\mathrm{u}]\!]} = \int_{\gamma_{\mathrm{i}}} \mathbf{N}_{[\![\mathrm{u}]\!]}^{\mathrm{T}} \mathbf{T} \mathbf{N}_{[\![\mathrm{u}]\!]} d\gamma_{\mathrm{i}} \tag{10}$$

where $\mathbf{N}_{[\![\mathrm{u}]\!]}$ is the shape function matrix for displacement jumps, γ_{i} are the interface surfaces and $\mathbf{T}$ is the tangent constitutive matrix for the interface elements.

At the microscale, the constitutive model of each material component is assumed *a priori* and is used to compute the stresses $\boldsymbol{\sigma} = \boldsymbol{\sigma}(\boldsymbol{\epsilon})$, the tractions $\mathbf{t} = \mathbf{t}([\![\mathbf{u}]\!])$ and provide the tangent constitutive matrices:

$$\mathbf{D}_u = \frac{\partial \boldsymbol{\sigma}}{\partial \boldsymbol{\epsilon}} \qquad \mathbf{T} = \frac{\partial \mathbf{t}}{\partial [\![\mathbf{u}]\!]} \tag{11}$$

Since water affects each material component (fibre, matrix, interface) differently, suitable constitutive models have to be chosen in order to capture the essential degradation and failure processes that can occur during ageing. The fibres are modelled as linear-elastic and their failure is not considered. In the subsequent sections, the models for the epoxy and fibre-matrix interface behaviours are presented in detail.

2.3.1 Epoxy model

The epoxy resin is modelled as elasto-plastic with damage, using the model formulated by Melro *et al.* [22] and incorporating improvements proposed by Van der Meer [26]. The model is composed of a linear-elastic portion followed by plastic hardening and transitioning to damage with exponential softening after the fracture strength is reached.

The model starts as elasto-plastic, with a stress-strain relationship given by:

$$\sigma_{ij} = D_{ijkl}^{\mathrm{e}}\left(\epsilon_{kl} - \epsilon_{kl}^{\mathrm{p}}\right) \tag{12}$$

where only the elastic part of the strains is considered and the elastic stiffness D_{ijkl} can be written as:

$$D_{ijkl} = G(\delta_{ij}\delta_{kl} + \delta_{il}\delta_{jk}) + \left(K - \frac{2}{3}G\right)\delta_{ij}\delta_{kl} \tag{13}$$

with K being the bulk modulus for the resin and G its shear modulus. Plastic strains develop when the yield surface is reached. A paraboloidal surface is considered:

$$\phi^{\mathrm{p}}(\boldsymbol{\sigma}, \sigma_{\mathrm{c}}, \sigma_{\mathrm{t}}) = 6J_2 + 2I_1(\sigma_{\mathrm{c}} - \sigma_{\mathrm{t}}) - 2\sigma_{\mathrm{c}}\sigma_{\mathrm{t}} \leq 0 \tag{14}$$

where σ_{c} and σ_{t} are the compression and tension yield stresses, respectively, J_2 is the second invariant of the deviatoric stress tensor and I_1 is the first stress invariant. This yield surface consists of the classic von Mises surface augmented with the pressure-dependent term $2I_1(\sigma_{\mathrm{c}} - \sigma_{\mathrm{t}})$.

The evolution of the yield surface due to hardening is dictated by the evolution of σ_{c} and σ_{t} with the equivalent plastic strain $\epsilon^{\mathrm{p}}_{\mathrm{eq}}$. At each time step, the variation of the equivalent plastic strain is given by:

$$\Delta\epsilon^{\mathrm{p}}_{\mathrm{eq}} = \sqrt{k\Delta\epsilon^{\mathrm{p}}_{ij}\Delta\epsilon^{\mathrm{p}}_{ij}} \;\; \Rightarrow \;\; \sigma_{\mathrm{c}} = \sigma_{\mathrm{c}}(\epsilon^{\mathrm{p}}_{\mathrm{eq}}),\, \sigma_{\mathrm{t}} = \sigma_{\mathrm{t}}(\epsilon^{\mathrm{p}}_{\mathrm{eq}}) \tag{15}$$

and the variation of the plastic strains is computed through a non-associative flow rule given by:

$$\Delta\epsilon^{\mathrm{p}}_{ij} = \Delta\gamma\left(3S_{ij} + \frac{2}{9}\alpha I_1\delta_{ij}\right) \tag{16}$$

where S_{ij} is the deviatoric stress tensor and α depends on the plastic Poisson ratio ν_{p}:

$$\alpha = \frac{9}{2}\frac{1 - 2\nu_{\mathrm{p}}}{1 + \nu_{\mathrm{p}}} \tag{17}$$

In order to determine the plastic multiplier increment $\Delta\gamma$, an iterative elastic predictor/return mapping algorithm is used until the computed stress state stops violating the yield surface (*i.e.* until $\phi^{\mathrm{p}} = 0$). Details on the return mapping algorithm and on computing the consistent tangent matrix are left out of the present discussion for the sake of compactness and can be found in [26].

When the material fracture strength is reached, the model switches to a continuum damage formulation with secant unloading. After such point, the stress-strain relationship is given by:

$$\epsilon^{\mathrm{e}}_{ij} = \epsilon_{ij} - \epsilon^{\mathrm{p}}_{ij} = \frac{1 + \nu}{E(1 - d_{\mathrm{m}})}\sigma_{ij} - \frac{\nu d_{\mathrm{m}}}{E(1 - d_{\mathrm{m}})}\sigma_{ij}\delta_{ij} - \frac{\nu}{E}\sigma_{kk}\delta_{ij} \tag{18}$$

where the plastic strain is still subtracted from the total strain but stops evolving after damage starts developing. A single damage variable d_{m} is adopted and its evolution is dictated by the fracture surface defined as:

$$\phi^{\mathrm{d}}(\widetilde{\boldsymbol{\sigma}}, r) = 6\widetilde{J}_2 + 2\widetilde{I}_1(X_{\mathrm{c}} - X_{\mathrm{t}}) - 2rX_{\mathrm{c}}X_{\mathrm{t}} \leq 0 \tag{19}$$

which is similar to Eq. (14) but with yield stresses substituted by the fracture strengths (X_{c}, X_{t}) and the invariants are now computed with the effective stresses, calculated using the undamaged stiffness tensor of Eq. (13).

In order to ensure that the stress state does not violate the fracture surface, the internal variable r at time step t_n is:

$$r^{t_n} = \max\left\{1, \max_{0 \leq t \leq t_n}\left\{\frac{3\widetilde{J}^t_2}{X_{\mathrm{c}}X_{\mathrm{t}}} + \frac{\widetilde{I}^t_1(X_{\mathrm{c}} - X_{\mathrm{t}})}{X_{\mathrm{c}}X_{\mathrm{t}}}\right\}\right\} \tag{20}$$

and is related to the damage parameter d_{m} by:

$$d_{\mathrm{m}} = 1 - \frac{e^{A\left(3 - \sqrt{7 + 2r^2}\right)}}{\sqrt{7 + 2r^2} - 2} \tag{21}$$

where the parameter A is computed through the classic Crack Band model by regularising the dissipated energy with respect to the fracture toughness G_c and the characteristic length of the finite element l_{e}:

$$f(A) = \int_1^{\infty} \frac{\partial U}{\partial d_{\mathrm{m}}}\frac{\partial d_{\mathrm{m}}}{\partial r}dr = \frac{G_c}{l_{\mathrm{e}}} \tag{22}$$

with l_{e} computed as:

$$l^{\mathrm{2D}}_{\mathrm{e}} = \frac{6}{\pi\sqrt[4]{3}}\sqrt{\gamma_{\mathrm{e}}} \qquad l^{\mathrm{3D}}_{\mathrm{e}} = \sqrt[3]{\omega_{\mathrm{e}}} \tag{23}$$

and γ_{e} and ω_{e} are the element area and volume, respectively. The consistent tangent matrix is obtained through linearisation of the secant stress-strain expression of Eq. (18). Further details on the linearisation process can be found in [22].

2.3.2 Cohesive interface model

The occurrence of fibre-matrix interface debonding is simulated by incorporating a cohesive zone damage model to interface elements generated around every fibre of the RVE. The chosen model is a mixed-mode damage law developed by Turon *et al*. [23], with later improvements proposed by Van der Meer and Sluys [27]. In the local frame of the interface element, the traction-separation law can be written as:

$$\mathbf{t} = [\mathbf{I} - d_{\mathrm{i}}\mathbf{P}]K_{\mathrm{d}}[\![\mathbf{u}]\!] \tag{24}$$

where K_{d} is an initial stiffness, d_{i} is the damage variable associated with the model and the matrix $\mathbf{P}$ prevents the development of cohesive tractions in compression by applying the operator $\langle x \rangle = (x + |x|)/2$:

$$\mathbf{P} = \begin{bmatrix} \frac{\langle [\![u]\!]_n \rangle}{[\![u]\!]_n} & 0 & 0 \\ 0 & 1 & 0 \\ 0 & 0 & 1 \end{bmatrix} \tag{25}$$

where $[\![u]\!]_n$ is the displacement jump in the direction normal to the interface surfaces.

The damage variable d_{i} is given by:

$$d_{\mathrm{i}}^{t_n} = \max_{0 \le t \le t_n} \begin{cases} 0, & [\![u]\!]_{\mathrm{eq}} \le [\![u]\!]_{\mathrm{eq}}^0 \\ \frac{[\![u]\!]_{\mathrm{eq}}^{\mathrm{f}}([\![u]\!]_{\mathrm{eq}} - [\![u]\!]_{\mathrm{eq}}^0)}{[\![u]\!]_{\mathrm{eq}}([\![u]\!]_{\mathrm{eq}}^{\mathrm{f}} - [\![u]\!]_{\mathrm{eq}}^0)}, & [\![u]\!]_{\mathrm{eq}}^0 < [\![u]\!]_{\mathrm{eq}} < [\![u]\!]_{\mathrm{eq}}^{\mathrm{f}} \\ 1, & [\![u]\!]_{\mathrm{eq}} \ge [\![u]\!]_{\mathrm{eq}}^{\mathrm{f}} \end{cases} \tag{26}$$

where the equivalent displacement jump ($[\![u]\!]_{\mathrm{eq}}$), the displacement jump at the onset of damage ($[\![u]\!]_{\mathrm{eq}}^0$) and the jump after damage has completely developed ($[\![u]\!]_{\mathrm{eq}}^{\mathrm{f}}$) are given by:

$$[\![u]\!]_{\mathrm{eq}} = \sqrt{\langle [\![u]\!]_n \rangle^2 + [\![u]\!]_{\mathrm{sh}}^2} \qquad [\![u]\!]_{\mathrm{sh}}^2 = [\![u]\!]_s^2 + [\![u]\!]_t^2 \tag{27}$$

$$[\![u]\!]_{\mathrm{eq}}^0 = \sqrt{([\![u]\!]_n^0)^2 + \chi^\eta \left[([\![u]\!]_s^0)^2 - ([\![u]\!]_n^0)^2 \right]} \tag{28}$$

$$[\![u]\!]_{\mathrm{eq}}^{\mathrm{f}} = \frac{[\![u]\!]_n^0 [\![u]\!]_n^{\mathrm{f}} + \chi^\eta \left[[\![u]\!]_s^0 [\![u]\!]_s^{\mathrm{f}} - [\![u]\!]_n^0 [\![u]\!]_n^{\mathrm{f}} \right]}{[\![u]\!]_{\mathrm{eq}}^0} \tag{29}$$

where η is the Benzeggagh-Kenane mode interaction parameter [28] and χ is the ratio between the shear energy dissipation and the total dissipation:

$$\chi = \frac{[\![u]\!]_{\mathrm{sh}}^2}{[\![u]\!]_{\mathrm{sh}}^2 + \langle [\![u]\!]_n \rangle^2} \tag{30}$$

Finally, the single-mode displacement jumps at damage onset depend on the fracture strength of the interface while the final interface openings depend on its fracture toughness:

$$[\![u]\!]_n^0 = \frac{X_n}{K_{\mathrm{d}}} \qquad [\![u]\!]_s^0 = \frac{X_s}{K_{\mathrm{d}}} \qquad [\![u]\!]_n^{\mathrm{f}} = \frac{2G_{Ic}}{X_n} \qquad [\![u]\!]_s^{\mathrm{f}} = \frac{2G_{IIc}}{X_s} \tag{31}$$

The formulation is completed with the definition of the material tangent stiffness matrix $\mathbf{T}$ of Eq. (11) through consistent linearisation of the traction-separation law of Eq. (24). Details of the linearisation procedure can be found in [27].

2.3.3 Loads and boundary conditions

In the present model, periodic boundary conditions are adopted in the micromodel in order to represent the behaviour of a macroscopic bulk material point. Figure 2 shows a schematic representation of the node groups involved in enforcing the boundary conditions. The origin of the RVE coordinate system is fixed at node 0 and its displacement is fixed:

$$\mathbf{u}_0 = \mathbf{0} \tag{32}$$

The corner nodes with displacements given by $\mathbf{u}_j^c$, where j ranges from 1 to the number of spatial dimensions of the RVE, will be prescribed based on the macroscopic strain values at the point according to

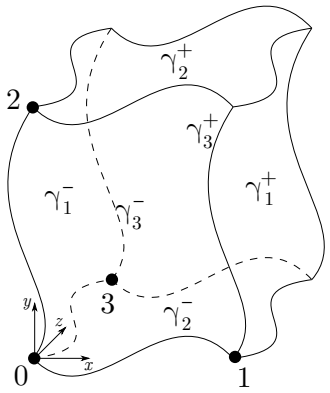

Figure 2: Periodic RVE with controlling nodes and boundary surfaces.

the scale transitions discussed in Section 2.4. Finally, the displacements of nodes on opposing boundary surfaces are related by:

$$\mathbf{u}^{\gamma_j^+} = \mathbf{u}^{\gamma_j^-} + \mathbf{u}_j^c \tag{33}$$

where the constraints are handled using the master-slave method, which means that the degrees of freedom of the slave nodes will be condensed out of the microscopic global stiffness matrix.

Resin elements are allowed to swell based on the current water concentration of the micromodel. The swelling is applied as a strain contribution at each material point:

$$\epsilon_{ij}^{\text{total}} = \epsilon_{ij} - c\alpha_{\text{sw}}\delta_{ij} \tag{34}$$

where α_{sw} is the swelling coefficient of the resin. Since the fibres do not take water and are therefore not allowed to swell, differential swelling stresses will be generated. If the RVE is free to swell, the volume average of such stresses will be zero. However, the presence of prescribed macroscopic strains on the RVE implies that the micromodel cannot swell freely, and the resultant modified stress field may bring changes to its failure behaviour.

2.3.4 Concentration-dependent properties

Experimental evidence shows a significant drop in mechanical properties of the resin and interface after water uptake [7, 2]. In order to realistically predict the effects of the ageing process, such degradation caused by plasticization and interfacial bond weakening must be incorporated in the micromodel. Here, resin and interface properties are linearly dependent on the water concentration of the micromodel using a single degradation factor:

$$d_{\text{w}} = \frac{d_{\text{w}}^{\infty}}{c_{\infty}} c \tag{35}$$

where c_{∞} and d_{w}^{∞} are respectively the water concentration and associated material degradation at saturation, obtained experimentally.

With the definition of the degradation factor, the resin properties are modified as:

$$E^{\text{w}} = (1 - d_{\text{w}})E, \;\; \sigma_{\text{c}}^{\text{w}} = (1 - d_{\text{w}})\sigma_{\text{c}}, \;\; \sigma_{\text{t}}^{\text{w}} = (1 - d_{\text{w}})\sigma_{\text{t}} \tag{36}$$

$$X_{\text{c}}^{\text{w}} = (1 - d_{\text{w}})X_{\text{c}}, \;\; X_{\text{t}}^{\text{w}} = (1 - d_{\text{w}})X_{\text{t}}, \;\; G_c^{\text{w}} = (1 - d_{\text{w}})^2 G_c \tag{37}$$

and the interface properties as:

$$X_n^{\text{w}} = (1 - d_{\text{w}})X_n, \;\; X_s^{\text{w}} = (1 - d_{\text{w}})X_s, \;\; G_{Ic}^{\text{w}} = (1 - d_{\text{w}})^2 G_{Ic}, \;\; G_{IIc}^{\text{w}} = (1 - d_{\text{w}})^2 G_{IIc} \tag{38}$$

It is important to note that applying the degradation factor to the yield stresses σ_{c} and σ_{t} implies a degradation of the hardening curve for every value of equivalent plastic strain. For fracture toughness, the squared degradation factor was adopted for the sake of numerical stability and implies reductions in both the strength and the strain (or displacement jump) level at which the softening is completely developed.

2.4 Scale transitions

With the formulations of the models in both macro- and microscales, it is necessary to define the interaction between scales. Following the scheme presented in Figure 1, such interactions comprise a macro-to-micro downscaling procedure, where strain and water concentration are passed to the micromodels, and a micro-to-macro upscaling procedure, with the recovery of the macroscopic stress and tangent stiffness.

Starting with the downscaling procedure, the displacement field of the micromodel can be decomposed in a linear displacement field related to the macroscopic strain and a fluctuation field $\widetilde{u}$ caused by microscopic inhomogeneities:

$$u_i^{\mathrm{m}} = \epsilon_{ij}^{\mathrm{M}} x_j^{\mathrm{m}} + \widetilde{u}_i^{\mathrm{m}} \tag{39}$$

It is important to note that such linear dependency on the macroscopic strain is only allowed because the principle of separation of scales mentioned in Section 2.3 is considered valid. For water concentration, since it is directly linked to strains through swelling (Equation 34), bringing concentration gradients to the microscale would make it necessary to also bring strain gradients. This approach is not followed here and the concentration is therefore considered constant over the entire microscopic domain, a hypothesis also adopted by Terada and Kurumatani [18]:

$$c^{\mathrm{m}} = c^{\mathrm{M}}(\mathbf{x}^{\mathrm{M}}) \tag{40}$$

When making the transition to the microscale, the volume average of the microscopic strain must be equal to the macroscopic strain at a particular material point:

$$\epsilon_{ij}^{\mathrm{M}}(\mathbf{x}^{\mathrm{M}}) = \frac{1}{|\omega|}\int_{\omega} \epsilon_{ij}^{\mathrm{m}}(\mathbf{x}^{\mathrm{m}}) d\omega = \frac{1}{|\omega|}\int_{\gamma} (u_i^{\mathrm{m}} n_j + u_j^{\mathrm{m}} n_i) d\gamma \tag{41}$$

where the volume integral was substituted by one in the RVE surface γ using the Gauss theorem and $\mathbf{n}$ is the vector normal to γ. Substituting Eq. (39), we obtain:

$$\frac{1}{|\omega|}\int_{\gamma} (\widetilde{u}_i^{\mathrm{m}} n_j + \widetilde{u}_j^{\mathrm{m}} n_i) d\gamma = 0 \quad \Rightarrow \quad \epsilon_{ij}^{\mathrm{M}} = \frac{1}{|\omega|}\int_{\omega} \epsilon_{ij}^{\mathrm{m}} d\omega \tag{42}$$

which dictates that the strain averaging is only satisfied if the fluctuation displacement field cancels at the RVE boundary.

After solving the microscopic boundary value problem, the macroscopic stress tensor must be recovered from the micro solution. For this part of the upscaling procedure, the Hill-Mandel principle is applied:

$$\sigma_{ij}^{\mathrm{M}} \dot{\epsilon}_{ij}^{\mathrm{M}} = \frac{1}{|\omega|}\int_{\omega} \sigma_{ij}^{\mathrm{m}} \dot{\epsilon}_{ij}^{\mathrm{m}} d\omega = \frac{1}{|\omega|}\int_{\gamma} t_i^{\mathrm{m}} \dot{u}_i^{\mathrm{m}} d\gamma \tag{43}$$

The principle postulates that the macroscopic stress power must be equal to the volume average of the microscopic one. The volume integral can be substituted by a boundary integral of the product between the traction and the variation of the displacement field. Substituting Eq. (39), we obtain a result similar to the one in Eq. (42):

$$\frac{1}{|\omega|}\int_{\gamma} t_i^{\mathrm{m}} \dot{\widetilde{u}}_i^{\mathrm{m}} d\gamma = 0 \quad \Rightarrow \quad \sigma_{ij}^{\mathrm{M}} = \frac{1}{|\omega|}\int_{\omega} \sigma_{ij}^{\mathrm{m}} d\omega \tag{44}$$

which means that the microscopic fluctuation field must have zero resultant work at the boundaries.

Considering the periodic boundary conditions shown in the previous section and imposing the additional requirement that the geometry of the RVE must be symmetric, it can be shown that:

$$\widetilde{u}_i^{\mathrm{m}+} = \widetilde{u}_i^{\mathrm{m}-} \qquad n_i^{+} = -n_i^{-} \qquad t_i^{\mathrm{m}+} = -t_i^{\mathrm{m}-} \tag{45}$$

from which the following equalities arise:

$$\int_{\gamma^-} (\widetilde{u}_i^{\mathrm{m}-} n_j^{-} + \widetilde{u}_j^{\mathrm{m}-} n_i^{-}) d\gamma = -\int_{\gamma^+} (\widetilde{u}_i^{\mathrm{m}+} n_j^{+} + \widetilde{u}_j^{\mathrm{m}+} n_i^{+}) d\gamma \tag{46}$$

$$\int_{\gamma^-} \dot{\widetilde{u}}_i^{\mathrm{m}-} t_i^{\mathrm{m}-} d\gamma = -\int_{\gamma^+} \dot{\widetilde{u}}_i^{\mathrm{m}+} t_i^{\mathrm{m}+} d\gamma \tag{47}$$

Substituting Eqs. (46) and (47) into Eqs. (42) and (41), it can be seen that both requirements for the fluctuation field are satisfied.

Finally, the scale transitions can be formulated in Voigt notation for ease of implementation. For a given macroscopic strain tensor $\boldsymbol{\epsilon}^{\mathrm{M}}$, the displacements $\mathbf{u}_j^c$ of the controlling nodes shown in Figure 2 are computed as:

$$\mathbf{u}_j^c = \mathbf{H}_j^{\mathrm{T}} \boldsymbol{\epsilon}^{\mathrm{M}}, \qquad \mathbf{H}_j = \frac{1}{2} \begin{bmatrix} 2x & 0 & 0 \\ 0 & 2y & 0 \\ 0 & 0 & 2z \\ y & x & 0 \\ 0 & z & y \\ z & 0 & x \end{bmatrix}_j, \boldsymbol{\epsilon}^{\mathrm{M}} = \begin{bmatrix} \epsilon_{xx}^{\mathrm{M}} \\ \epsilon_{yy}^{\mathrm{M}} \\ \epsilon_{zz}^{\mathrm{M}} \\ 2\epsilon_{xy}^{\mathrm{M}} \\ 2\epsilon_{yz}^{\mathrm{M}} \\ 2\epsilon_{xz}^{\mathrm{M}} \end{bmatrix} \tag{48}$$

where the matrix $\mathbf{H}$ is filled with the coordinates of each controlling node. After solving the microscopic equilibrium equations and obtaining the internal forces at the controlling nodes, the macroscopic stresses are recovered:

$$\boldsymbol{\sigma}^{\mathrm{M}} = \frac{1}{|\omega|} \begin{bmatrix} \mathbf{H}_1 & \mathbf{H}_2 & \mathbf{H}_3 \end{bmatrix} \begin{bmatrix} \mathbf{f}_1^{\mathrm{m}} \\ \mathbf{f}_2^{\mathrm{m}} \\ \mathbf{f}_3^{\mathrm{m}} \end{bmatrix} = \frac{1}{|\omega|} \mathbf{H} \mathbf{f}_{\mathrm{c}}^{\mathrm{m}} \tag{49}$$

The final step in the upscaling procedure is to compute the tangent macroscopic stiffness matrix $\delta\boldsymbol{\sigma}^{\mathrm{M}} = \mathbf{D}_u^{\mathrm{M}} \delta\boldsymbol{\epsilon}^{\mathrm{M}}$ from Eq. (8). Here, the procedure follows the formulation presented by Nguyen *et al.* [14] but is rewritten for the case of homogenization towards a bulk macroscopic point. The procedure starts by partitioning the global stiffness matrix of the micromodel as follows:

$$\begin{bmatrix} \mathbf{K}_{\mathrm{ii}}^{\mathrm{m}} & \mathbf{K}_{\mathrm{id}}^{\mathrm{m}} \\ \mathbf{K}_{\mathrm{di}}^{\mathrm{m}} & \mathbf{K}_{\mathrm{dd}}^{\mathrm{m}} \end{bmatrix} \begin{bmatrix} \delta\mathbf{u}_{\mathrm{i}}^{\mathrm{m}} \\ \delta\mathbf{u}_{\mathrm{d}}^{\mathrm{m}} \end{bmatrix} = \begin{bmatrix} \mathbf{r}_{\mathrm{i}}^{\mathrm{m}} \\ \mathbf{r}_{\mathrm{d}}^{\mathrm{m}} \end{bmatrix} \tag{50}$$

with d representing the dependent nodes from the slave surfaces (Figure 2) and i the remaining ones, including the controlling corner nodes. Representing the constraints by a coefficient matrix $\mathbf{C}$, the displacement vector is given by:

$$\begin{bmatrix} \delta\mathbf{u}_{\mathrm{i}}^{\mathrm{m}} \\ \delta\mathbf{u}_{\mathrm{d}}^{\mathrm{m}} \end{bmatrix} = \begin{bmatrix} \mathbf{I} \\ \mathbf{C} \end{bmatrix} \delta\mathbf{u}_{\mathrm{i}}^{\mathrm{m}} = \mathbf{T} \delta\mathbf{u}_{\mathrm{i}}^{\mathrm{m}} \tag{51}$$

Pre-multiplying both sides of Eq. (50) by $\mathbf{T}^{\mathrm{T}}$ and substituting the displacement vector by the one in Eq. (51), the dependent displacements are condensed out and a reduced system is obtained:

$$\begin{bmatrix} \overline{\mathbf{K}}^{\mathrm{m}} & \mathbf{0} \\ \mathbf{0} & \mathbf{I} \end{bmatrix} \begin{bmatrix} \delta\mathbf{u}_{\mathrm{i}}^{\mathrm{m}} \\ \delta\mathbf{u}_{\mathrm{d}}^{\mathrm{m}} \end{bmatrix} = \begin{bmatrix} \overline{\mathbf{r}}^{\mathrm{m}} \\ \delta\mathbf{u}_{\mathrm{d}}^{\mathrm{m}} \end{bmatrix}, \qquad \overline{\mathbf{K}}^{\mathrm{m}} = \mathbf{T}^{\mathrm{T}} \mathbf{K}^{\mathrm{m}} \mathbf{T}, \qquad \overline{\mathbf{r}}^{\mathrm{m}} = \mathbf{T}^{\mathrm{T}} \mathbf{r}^{\mathrm{m}} \tag{52}$$

The system is further partitioned by separating the controlling nodes (c) from the rest (a):

$$\begin{bmatrix} \overline{\mathbf{K}}_{\mathrm{aa}}^{\mathrm{m}} & \overline{\mathbf{K}}_{\mathrm{ac}}^{\mathrm{m}} \\ \overline{\mathbf{K}}_{\mathrm{ca}}^{\mathrm{m}} & \overline{\mathbf{K}}_{\mathrm{cc}}^{\mathrm{m}} \end{bmatrix} \begin{bmatrix} \delta\mathbf{u}_{\mathrm{a}}^{\mathrm{m}} \\ \delta\mathbf{u}_{\mathrm{c}}^{\mathrm{m}} \end{bmatrix} = \begin{bmatrix} \mathbf{0} \\ \delta\mathbf{f}_{\mathrm{c}}^{\mathrm{m}} \end{bmatrix} \tag{53}$$

where the variation of the external force on the controlling nodes used in the stress upscaling of Eq. (49) now appears in the right-hand side. From this reduced system, the macroscopic tangent stiffness matrix can be evaluated in a columnwise manner by using a probing technique:

$$\mathbf{D}_u^{\mathrm{M}} = \begin{bmatrix} \mathbf{D}_1^{\mathrm{M}} & \mathbf{D}_2^{\mathrm{M}} \cdots \mathbf{D}_n^{\mathrm{M}} \end{bmatrix}, \qquad \mathbf{D}_j^{\mathrm{M}} = \frac{1}{|\omega|} \mathbf{H}(\boldsymbol{\xi} - \boldsymbol{\lambda}) \tag{54}$$

where each column $j = 1, ..., n$ gives the stiffness contribution of one of the n strain components. The matrix $\mathbf{H}$ is given in Eq. (48) and the vectors $\boldsymbol{\xi}$ and $\boldsymbol{\lambda}$ are given by a sequence of matrix-vector multiplications:

$$\boldsymbol{\xi} = \overline{\mathbf{K}}_{\mathrm{cc}}^{\mathrm{m}} \boldsymbol{\beta}, \qquad \boldsymbol{\beta} = \mathbf{H}\mathbf{e}_j, \qquad \boldsymbol{\lambda} = \overline{\mathbf{K}}_{\mathrm{ca}}^{\mathrm{m}} \boldsymbol{\kappa}, \tag{55}$$

with $\mathbf{e}_j$ being the j-th row of an identity matrix of size n and $\boldsymbol{\lambda}$ is obtained by solving the linear system:

$$\begin{bmatrix} \overline{\mathbf{K}}_{\mathrm{aa}}^{\mathrm{m}} & \overline{\mathbf{K}}_{\mathrm{ac}}^{\mathrm{m}} \\ \overline{\mathbf{K}}_{\mathrm{ca}}^{\mathrm{m}} & \overline{\mathbf{K}}_{\mathrm{cc}}^{\mathrm{m}} \end{bmatrix} \begin{bmatrix} \boldsymbol{\kappa} \\ \mathbf{0} \end{bmatrix} = \begin{bmatrix} \overline{\mathbf{K}}_{\mathrm{ac}}^{\mathrm{m}} \boldsymbol{\beta} \\ \mathbf{0} \end{bmatrix} \tag{56}$$

which completes the definition of the macroscopic tangent stiffness without the need to invert the microscopic global stiffness matrix.

2.5 Solution methods

Using the multiphysics/multiscale numerical framework presented in the previous sections requires robust and efficient solution methods. For the diffusion analysis, a time stepping procedure is necessary, while a non-linear path-following method has to be used in the FE^2 stress analysis.

To solve the transient diffusion problem, the linear 3-step method developed by Park [29] is used. The water concentration field at time t is computed as [30]:

$$\mathbf{c}_t = h_\beta \dot{\mathbf{c}}_t + \mathbf{h}_t \tag{57}$$

where h_β is the scaled time step and $\mathbf{h}$ is a history vector that depends on the concentration fields of the three previous steps.

For the stress analysis, a Newton-Raphson solver is applied. During the ageing process, the non-linear equilibrium problem is solved for each time step and a path-following algorithm is not needed. For every macroscopic iteration, the microscopic equilibrium problem has to be solved at every material point. Since the points are independent from one another, they are solved in parallel in a shared-memory environment. For material points close to the surfaces exposed to water, saturation happens in one time step, which can make convergence difficult. In order to mitigate this issue, the substepping algorithm proposed by Sommer *et al*. [31] is applied. Here, the method is modified by splitting not only the macroscopic strains but also the water concentration in two consecutive substeps. If no convergence is obtained for any of the substeps, the process is repeated recursively.

At the end of the ageing process, it is interesting to assess the strength degradation caused by water immersion by loading each material point to failure and obtaining their failure envelopes. For this type of analysis, the dissipation-based arclength method developed by Gutiérrez is used [32]. The method constrains the dissipated energy during one time step by imposing the constraint:

$$\frac{1}{2}\Big(\lambda_0 \Delta\overline{\mathbf{u}}^{\mathrm{T}}\mathbf{q} - \Delta\lambda\overline{\mathbf{u}}_0^{\mathrm{T}}\mathbf{q} + \Delta\overline{\mathbf{u}}^{\mathrm{T}}\mathbf{f}_0^*\Big) = \Delta U \tag{58}$$

where λ is the load factor, $\mathbf{q}$ is the unit load vector and the subscript 0 indicates values from the last converged time step. The term $\Delta\overline{\mathbf{u}}^{\mathrm{T}}\mathbf{f}_0^*$ was proposed by Van der Meer *et al*. [33] and accounts for the presence of permanent plastic deformations and swelling strains. The dissipated energy ΔU is adjusted during the analysis by an efficient adaptive stepping algorithm [34].

Since a continuum damage model regularised using the Crack Band method is used for the epoxy at the microscale, additional convergence problems arise as the Newton-Raphson solver struggles to identify which band of elements is damaging and gets trapped in an oscillatory response. To restore convergence in such cases, the modified Newton-Raphson scheme proposed by Van der Meer [34] is used, in which the oscillating points are identified and their secant stiffness is used instead of the consistent tangent one. After the residual decreases for a certain number of consecutive steps, the algorithm switches back to using the consistent tangent.

3 Results

The presented numerical framework is used to model the hygrothermal ageing behaviour of unidirectional composite laminates. In the examples presented in this section, a glass/epoxy material system used in wind turbine design (EPIKOTE RIMR135/1366 resin and PPG Hybon 2002 glass fibre rovings) is considered. The material properties for each of the constituents (fibre, matrix and interface) are shown in Table 1.

For the resin, most properties were obtained experimentally on neat resin specimens tested in tension and compression. The resultant stress-strain curves were also used to extract the plastic hardening curves, shown in Figure 3. Properties for the glass fibre and fibre/matrix interface were obtained from literature. The maximum uptake c_∞ and diffusivity (D) for the unidirectional composite material were obtained through an immersion experiment in water at 50°C, with weight measurements performed periodically [35]. Finally, the maximum property degradation at saturation (d_{w}^∞) was obtained from mechanical tests on saturated tension specimens.

The proposed model for concentration dependency of Section 2.3.4 was validated using experimental results on saturated epoxy. Figure 4 shows results of 1-element models, where the purple and red curves were obtained using the hardening curves extracted from compression and tension tests on dry resin specimens, respectively. For these two cases, a good agreement between experiments and models is expected since the original curves were used to calibrate the model. The blue curve was obtained by degrading the dry model using $d_{\mathrm{w}} = 0.2$. The good agreement with the experimental curve of a saturated specimen

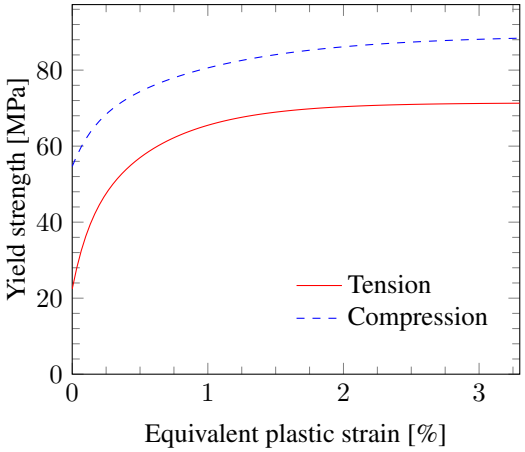

Figure 3: Input hardening data for the epoxy model.

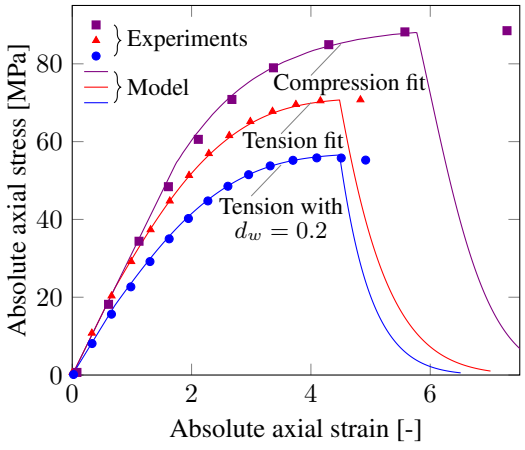

Figure 4: Experimental validation of the epoxy model.

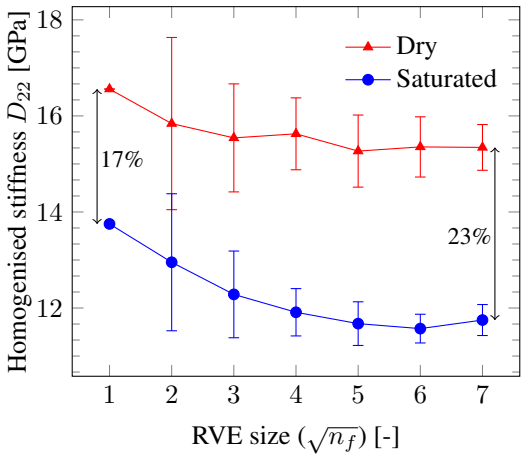

Figure 5: Stiffness changes with RVE size.

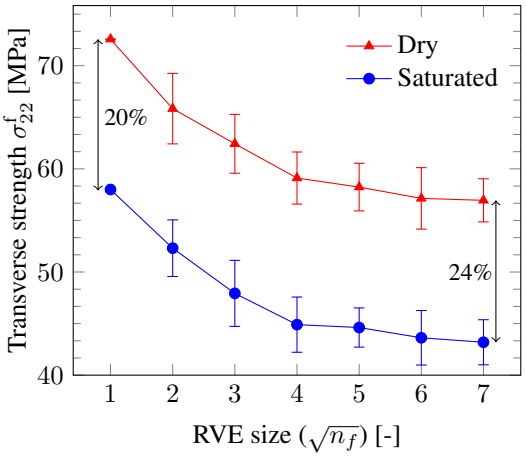

Figure 6: Transverse tension strength changes with RVE size.

shows that using a single degradation factor for stiffness, yield stress and strength is effective for describing the degradation in the material response, although no conclusion can be drawn about the adopted fracture toughness degradation due to the sudden failure behaviour of the specimens.

3.1 RVE study

In applying the proposed formulation, it is important to choose a suitable RVE size. In order to be representative, the RVE should be large enough to ensure that the micromodel response does not change considerably if the size is further increased. In this work, two-dimensional micromodels with random fibre distributions are used. Simplification of the presented three-dimensional formulations of Section 2 for a 2D analysis is trivial and will not be presented.

The models were generated using the discrete element package HADES, starting with a regular grid of circles representing the fibres, bounded by a periodic box. A pseudo-random velocity vector is assigned to each circle and a contact model is executed, letting the circles get rearranged as they collide, while the bounding box shrinks over time. The process is stopped when the desired fibre volume fraction is reached. The resultant geometry is then meshed with triangular finite elements using Gmsh [36]. Based on loss-on-ignition measurements and microscopic observations on the adopted material system, the fibre diameter was randomly generated between 13 μm and 16 μm and a target volume fraction of 0.6 was adopted. Interface elements are generated at runtime around every fibre.

Figure 5 shows homogenised stiffness values for micromodels with a number of fibres ranging from 4 (2 x 2) to 49 (7 x 7), including a unit cell with one fibre and surrounding matrix. Values for both dry and saturated micromodels are shown and each point shows the average and standard deviation obtained using 30 different micromodels (with the exception of unit cell values).

Epoxy		Interface		Fibre		Diffusion	
E [kPa] [a]	3130	K_{d} [kPa] [b]	$5 \cdot 10^7$	E [kPa] [37]	73000	c_∞ [%] [a]	3.4
ν [-] [a]	0.37	X_n [kPa] [38]	60.0	ν [-] [37]	0.22	D [µm^2/s] [a]	0.500
ν_{p} [-] [a]	0.32	X_s [kPa] [38]	60.0				
X_{t} [kPa] [a]	70.7	G_{Ic} [N/mm] [38]	0.87				
X_{c} [kPa] [a]	88.5	G_{IIc} [N/mm] [38]	1.72				
G_c [N/mm] [22]	0.09	η [-] [b]	1.0				
α_{sw} [%$^{-1}$] [a]	0.002	d_{w}^{∞} [-] [b]	0.2				
d_{w}^{∞} [-] [a]	0.2						

[a] Values experimentally obtained by the authors.
[b] Assumed values.

Table 1: Material Properties used in the examples.

As the size of the RVE is increased, average stiffness values for both dry and wet models tend to decrease. The standard deviation also decreases, although significant scatter is still observed even for the largest RVE size considered, which is partly due to fluctuations in the obtained fibre volume fraction after the discrete element contact analysis.

It is interesting to note that the difference between wet and dry stiffness values increases as the RVE grows in size, with a 17% reduction obtained for the unit cell model and a 23% one for 7 x 7 models, on average. The difference in the rate of stiffness reduction with RVE size is caused by failure events driven by the combination of swelling and degradation of the resin and interface properties. These failure events are not fully captured in smaller micromodels, making the convergence to a stable stiffness value slower when compared to dry micromodels.

The micromodels were also loaded in transverse tension (σ_{22}), with changes in strength as the RVE size increases shown in Figure 6. A behaviour similar to the one obtained for stiffness is observed, with a decrease in strength as the RVE size increases, although the convergence rate is now similar for both dry and wet micromodels. In general, a representive initial stiffness can be achieved with a relatively small RVE size, while correctly representing its failure behaviour both in terms of distributed and localised damage requires larger RVE sizes. Nevertheless, since significant scatter is still present for both stiffness and strength even for the largest RVE size considered in the present study, it cannot be claimed that a truly representative micromodel was found.

It is also interesting to investigate changes in failure behaviour after ageing for stress states other than uniaxial transverse tension. Figure 7 shows biaxial failure envelopes in both dry and wet conditions of a 7 x 7 RVE. Each point in the envelope was obtained by applying a horizontal load of $\lambda \cos\theta$ to controlling node 1 and a vertical load of $\lambda \sin\theta$ to controlling node 2 (see Figure 2), with θ ranging from 0° to 345° in steps of 15°. The load scale factor λ is resolved in every time step using the arc length method. For each direction, the strength was identified as the point that maximises $\sqrt{\sigma_{22}^2 + \sigma_{33}^2}$.

Comparing the obtained envelopes, it is interesting to note the differences in the wet material behaviour in tension and compression. For tension, a strength reduction of approximately 27% was obtained after ageing. In compression, however, the strength reduction falls to 15% due to the effect of differential swelling. This effect is particularly relevant for the case of biaxial compression ($\theta = 225°$), for which the wet strength is actually higher than the dry one, in spite of the weakening effect caused by plasticization and interface weakening. The resultant change in envelope shape after ageing can therefore be interpreted as the combination of shrinkage caused by water degradation and a shift caused by differential swelling.

It can therefore be concluded that in order to realistically model the hygrothermal ageing phenomenon in composites, it is important to take into account the contributions of both differential swelling and physical/chemical degradation. In isolation, neither mechanism is enough to represent the complex changes in failure behaviour after ageing.

3.2 Ageing example

The numerical framework presented in this work is demonstrated by simulating the hygrothermal ageing process in a unidirectional glass/epoxy composite specimen immersed in water at 50°C. The specimen di-

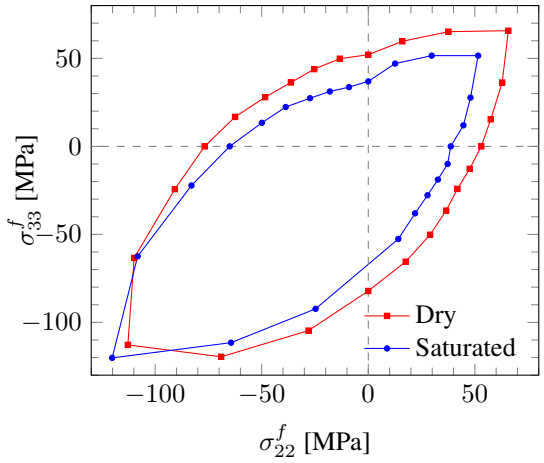

Figure 7: Biaxial failure envelopes for a 7 x 7 RVE, both dry and saturated.

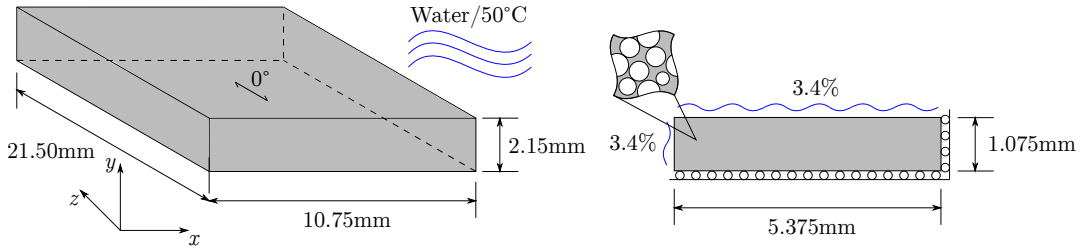

(a) Immersion problem

(b) Modelling approach

Figure 8: Modelling hygrothermal ageing in a unidirectional composite short-beam.

mensions and fibre direction are shown in Figure 8a, consisting in a short-beam typically used to evaluate the interlaminar shear strength of unidirectional composites in a three-point bending setup. Here, the virtual specimen is not mechanically loaded, and only the material degradation caused by the hygrothermal conditioning is simulated.

Figure 8b shows an idealised model of the ageing problem, where only the transverse plane of the specimen is modelled in plane strain and symmetry along the x and y axes is exploited in order to reduce the computational effort. With this modelling approach, it is assumed that diffusion and swelling do not occur along the z-axis. The latter assumption is reasonable since the specimen is significantly stiffer in the fibre direction, while the former leads to an underestimation of the water concentration field at any given time step, which is an acceptable drawback in exchange for computational efficiency. The specimen is initially dry and the immersion environment is simulated by prescribing the water concentration of pure resin at saturation to the top and left edges, while the bottom and right edges are mechanically constrained. A 5 x 5 RVE with strength response close to the average shown in Figure 6 was chosen to represent the material microscopic response.

The transient FE^2 problem is solved from $t = 0\,\text{h}$ to $t = 750\,\text{h}$, when saturation occurs, with a time step $h = 15\,\text{h}$. Figure 9 shows concentration and stress fields of the macromodel at three different time steps. The full field solution can be recovered from the symmetric model through mirroring along the x and y axes.

As expected, water concentration gradients along the specimen create transient tension, compression and shear stresses. These stresses attain peak values of 5 MPa in shear, 9 MPa in tension and 17 MPa in compression. The stress fields are consistent with the ones experimentally observed by Pitarresi *et al.* [10]. As diffusion progresses and the concentration gradients decrease, start to subside, vanishing upon saturation, as expected.

The effect of transient swelling in the microscopic material state can be visualised by tracking microscopic deformations throughout the ageing process. Figure 10 shows displacements and transverse stress fields (σ_{22}) of three distinct material points at three different time steps. Since the points are located close to the specimen surface, near-instant saturation is expected. However, the micromodels are constrained by the macroscopic compatibility requirement: Points 1 and 3 are constrained by neighboring dry points and can therefore only swell in one direction, while point 2 undergoes a combination of shear and swelling. At

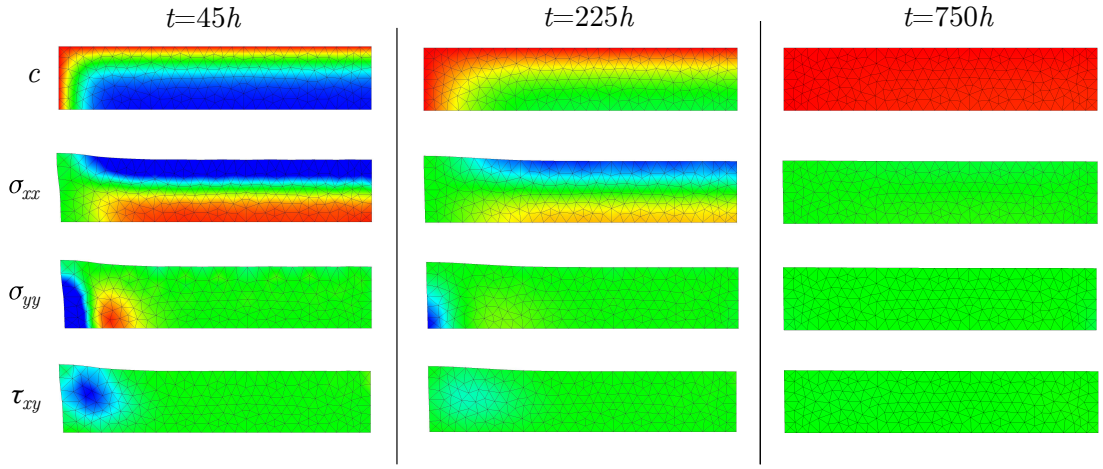

Figure 9: Evolution of macroscopic displacements and stresses during ageing.

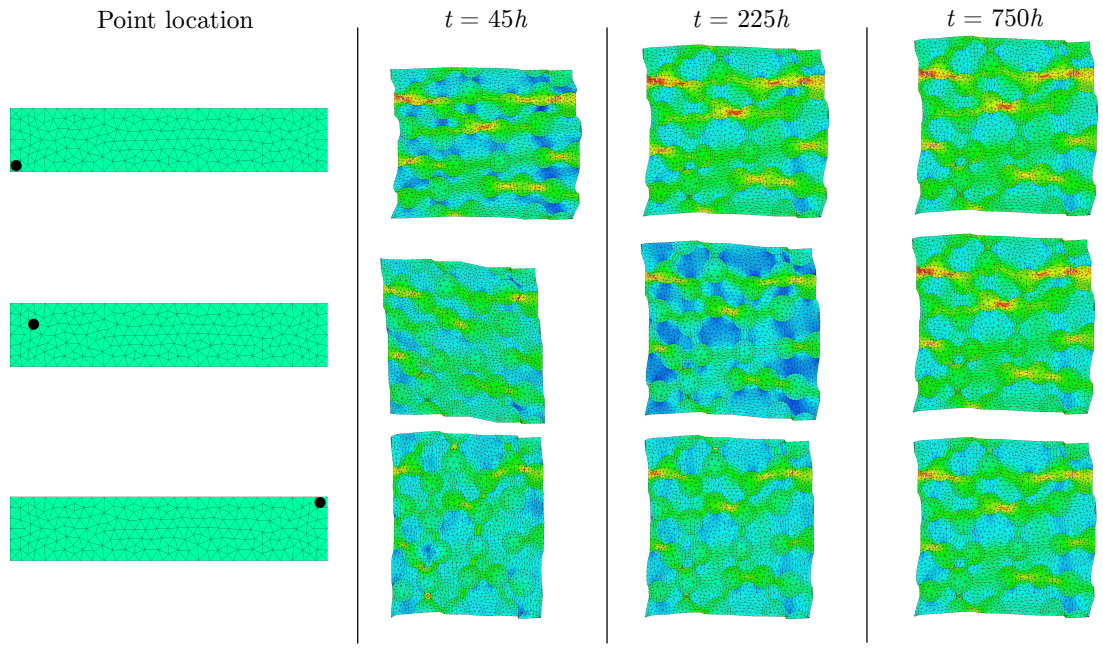

Figure 10: Evolution of microscopic displacements and transverse stresses for three different integration points.

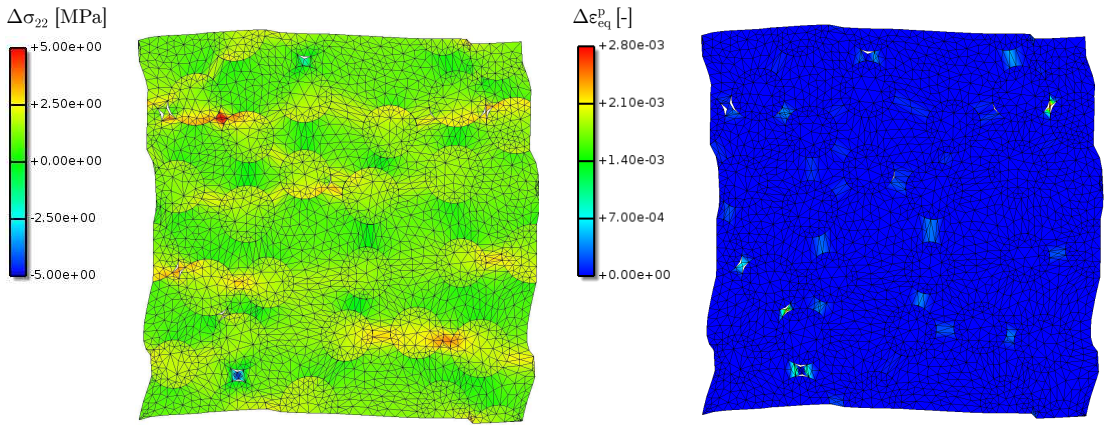

Figure 11: Difference fields obtained by superimposing the stress and plastic strain fields of two different saturated points.

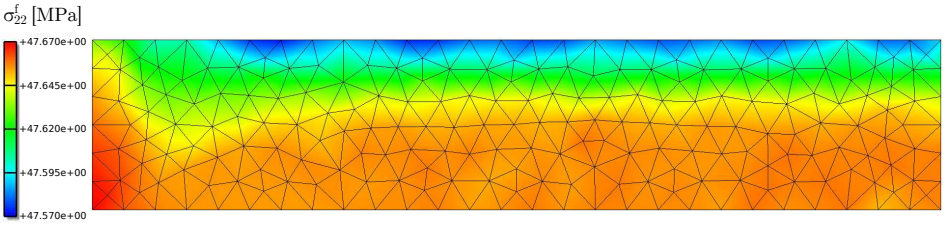

Figure 12: Spatial distribution of transverse tension strength in the macro specimen after ageing.

longer immersion times (750 h), the macroscopic stresses vanish and the points attain a similar deformed shape. However, because of the distinct strain history, equally saturated points can have different residual stress fields due to differences in local material state, as shown in Figure 11.

Besides tracking the material state during the ageing process in terms of stiffness degradation and distributed failure phenomena, it is also interesting to assess the strength degradation caused by exposure to water by mechanically loading the macroscopic specimen to failure. However, such analysis involves a number of incompatibilities with the presented numerical framework. Firstly, as the micromodel starts to exhibit global softening due to strain localisation, it can be proven that an RVE ceases to exist and the material response becomes more brittle as the micromodel size is increased [39]. Secondly, the periodic boundary conditions applied to the micromodels may impose additional constraints in the formation of a strain localisation band, depending on the direction of the external loading.

In this work, a simplified approach is taken in order to circumvent such incompatibilities. After the ageing analysis is completed (*i.e.* after the macromodel saturates), the displacement fields and material history of the micromodels are saved and used as the starting point of new analyses where mechanical loads are applied to the controlling nodes and the models are loaded until failure. Since an arc length method is used instead of resorting to displacement control, biaxial stress states can be simulated while keeping stress ratios constant. Stress values are then computed by averaging the nodal forces along the edges of the RVE. Since only the maximum stress is of interest, incompatibilities of the strain localisation band direction with the applied periodic boundary conditions have limited influence.

Such analysis approach can be used to obtain the spatial strength distribution of the macroscopic specimen after ageing, as can be seen in Figure 12 for uniaxial transverse tension σ_{22}. During ageing, the additional constraints imposed by transient swelling stresses and the consequent differences in development of distributed resin and interface failures create a non-uniform strength distribution. Although the difference in strength between the weakest and strongest points is small (approximately 200 kPa), the transient swelling effectively creates weak spots where damage is likely to initiate and propagate from. Such effect can only be captured by combining macroscopic diffusion with a fully-coupled multiscale mechanical analysis.

4 Conclusions

This work presented a coupled multiscale/multiphysics numerical analysis framework suitable for modelling of hygrothermal ageing in laminated composites. The proposed model consists of a macroscopic transient diffusion analysis coupled with a multiscale (FE^2) mechanical model in order to account for microscopic degradation mechanisms and failure events.

At the macroscale, diffusion is considered isotropic with constant diffusivity, while no mechanical constitutive model is explicitly defined. The mechanical response is instead obtained through homogenisation of the microscopic material response. At the microscale, diffusion is modelled as steady-state with constant water concentration. An elasto-plastic epoxy model with damage is combined with cohesive zones at the fibre/matrix interfaces in order to model failure caused by swelling, plasticization and interface weakening after water ingression. Detailed formulations for every constituent of the framework were presented.

While properties for the interfaces were obtained from literature, the calibration of the epoxy model has been performed based on experimental investigations in both dry and saturated pure resin specimens. It was shown that the water degradation model with a single degradation factor was capable of correctly predicting the experimental stress-strain material response after ageing.

An RVE size study was conducted, ranging from a unit cell model with a single fibre to 7 x 7 fibres micromodels with random fibre distribution. While the mean dry stiffness response stabilised with relatively small RVE sizes, the saturated stiffness and both dry and wet transverse strengths required larger sizes. Nevertheless, an RVE with representative behaviour could not be obtained in the investigated size range, since significant scatter was still present for both stiffness and strength. Biaxial transverse failure envelopes of both dry and saturated micromodels were also compared. After ageing, the failure envelope tends to shrink due to plasticization and interface weakening as well as shift towards the compression bisector due to differential swelling.

The capabilities of the model were demonstrated through the simulation of the hygrothermal ageing process of a unidirectional composite short-beam immersed in water at 50°C. Transient swelling stresses due to water concentration gradients were correctly predicted. Through the FE^2 scale coupling, the macroscopic compatibility requirement acted as constraints to the micromodels and influenced their final homogenised stiffness and strength. Although such transient effects were found to bring limited impact to the final material stiffness and strength, they effectively create weak spots where damage can initiate and propagate from.

Acknowledgements

The authors acknowledge the contribution of the TKI-WoZ and IRPWIND projects for motivating and partly funding this research and of the TKI-MIMIC project industrial partners for providing useful feedback.

References

[1] White JR, Turnbull TA. Review: Weathering of polymers: mechanisms of degradation and stabilization, test strategies and modelling. *Journal of Materials Science* 1994; **29**:584–613.

[2] Davies P, Mazéas F, Casari P. Sea water aging of glass reinforced composites: Shear behaviour and damage modelling. *Journal of Composite Materials* 2000; **35**(15):1343–1372.

[3] Joliff Y, Rekik W, Belec L, Chailan JF. Study of the moisture/stress effects on glass fibre/epoxy composite and the impact of the interphase area. *Composite Structures* 2014; **108**:876–885.

[4] Grammatikos SA, Zafari B, Evernden MC, Mottram JT, Mitchels JM. Moisture uptake characteristics of a pultruded fibre reinforced polymer flat sheet subjected to hot/wet aging. *Polymer Degradation and Stability* 2015; **121**:407–419.

[5] Gautier L, Mortaigne B, V B. Interface damage study of hydrothermally aged glass-fibre-reinforced polyester composites. *Composites Science and Technology* 1999; **59**:2329–2337.

[6] McBagonluri F, Garcia K, Hayes M, Verghese KNE, Lesko JJ. Characterization of fatigue and combined environment on durability performance of glass/vinyl ester composite for infrastructure applications. *International Journal of Fatigue* 2000; **22**:53–64.

[7] Naya F, González C, Lopes CS, van der Veen S, Pons F. Computational micromechanics of the transverse and shear behaviour of unidirectional fiber reinforced polymers including environmental effects. *Composites Part A - Applied Science and Manufacturing* 2016; .

[8] Haynes RA. *Hygrothermally stable laminated composites with optimal coupling*. PhD thesis, Georgia Institute of Technology, 2010.

[9] Koniorczyk M, Gawin D, Schrefler BA. Modeling evolution of frost damage in fully saturated porous materials exposed to variable hygro-thermal conditions. *Computer Methods in Applied Mechanics and Engineering* 2015; **297**:38–61.

[10] Pitarresi G, Scafidi M, Alessi S, Di Filippo M, Billaud C, Spadaro G. Absorption kinetics and swelling stresses in hydrothermally aged epoxies investigated by photoelastic image analysis. *Polymer Degradation and Stability* 2015; **111**:55–63.

[11] Geers MGD, Kouznetsova VG, Brekelmans WAM. Multi-scale computational homogenization: Trends and challenges. *Journal of Computational and Applied Mathematics* 2010; **234**:2175–2182.

[12] Miehe C, Schotte J, Schröder J. Computational micro-macro transitions and overall moduli in the analysis of polycrystals at large strains. *Computational Materials Science* 1999; **16**:372–382.

[13] Kouznetsova V, Brekelmans WAM, Baaijens FPT. An approach to micro-macro modeling of heterogeneous materials. *Computational Mechanics* 2001; **27**:37–48.

[14] Nguyen VP, Lloberas-Valls O, Stroeven M, Sluys LJ. Computational homogenization for multiscale crack modelling. implementation and computational aspects. *International Journal for Numerical Methods in Engineering* 2012; **89**:192–226.

[15] Crouch R, Oskay C, Clay S. Multiple spatio-temporal scale modeling of composites subjected to cyclic loading. *Computational Mechanics* 2013; **51**:93–107.

[16] Yu Q, Fish J. Multiscale asymptotic homogenization for multiphysics problems with multiple spatial and temporal scales: A coupled thermo-viscoelastic example problem. *International Journal of Solids and Structures* 2002; **39**:6429–6452.

[17] Özdemir I, Brekelmans WAM, Geers MGD. Computational homogenization for heat conduction in heterogeneous solids. *International Journal for Numerical Methods in Engineering* 2008; **73**:185–204.

[18] Terada K, Kurumatani M. Two-scale diffusion-deformation coupling model for material deterioration involving micro-crack propagation. *International Journal for Numerical Methods in Engineering* 2010; **83**:426–451.

[19] Yuan Z, Jiang T, Fish J, Morscher G. Reduced-order multiscale-multiphysics model for heterogeneous materials. *Journal for Multiscale Computational Engineering* 2014; **12**:45–64.

[20] Sengupta A, Papadopoulos P, Taylor RL. A multiscale finite element method for modeling fully coupled thermomechanical problems in solids. *International Journal for Numerical Methods in Engineering* 2012; **91**:1386–1405.

[21] Özdemir I, Brekelmans WAM, Geers MGD. Fe^2 computational homogenization for the thermomechanical analysis of heterogeneous solids. *Computer Methods in Applied Mechanics and Engineering* 2008; **198**:602–613.

[22] Melro AR, Camanho PP, Andrade Pires FM, Pinho ST. Micromechanical analysis of polymer composites reinforced by unidirectional fibres: Part I - Constitutive modelling. *International Journal of Solids and Structures* 2013; **50**:1897–1905.

[23] Turon A, Camanho PP, Costa J, Dávila CG. A damage model for the simulation of delamination in advanced composites under variable-mode loading. *Mechanics of Materials* 2006; **38**:1072–1089.

[24] Rocha IBCM, Raijmaekers S, Nijssen RPL, van der Meer F. Hydrothermal ageing of glass/epoxy composites for wind turbine blades. *In: Procedures of the 20th International Conference on Composite Materials*, 2015.

[25] El Yagoubi J, Lubineau G, Roger F, Verdu J. A fully coupled diffusion-reaction scheme for moisture sorption-desorption in an anhydride-cured epoxy resin. *Polymer* 2012; **53**:5582–5595.

[26] van der Meer FP. Micromechanical validation of a mesomodel for plasticity in composites. *European Journal of Mechanics - A/Solids* 2016; **60**:58–69.

[27] van der Meer FP, Sluys LJ. Mesh-independent modeling of both distributed and discrete matrix cracking in interaction with delamination in composites. *Engineering Fracture Mechanics* 2010; **77**:719–735.

[28] Benzeggagh ML, Kenane M. Measurement of mixed-mode delamination fracture toughness of unidirectional glass/epoxy composites with mixed mode bending apparatus. *Composites Science and Technology* 1996; **56**:439–449.

[29] Park KC. An improved stiffly stable method for direct integration of nonlinear structural dynamic equations. *Journal of Applied Mechanics* 1975; **42**:464–470.

[30] Remmers J. Mode-jumping simulations using the new implicit time integrator in b2000. *2nd B2000/MEMCOM workshop*, 1998.

[31] Sommer DD, de Souza Neto EA, Dettmer WG, Perić D. A sub-stepping scheme for multi-scale analysis of solids. *Computer Methods in Applied Mechanics and Engineering* 2009; **198**:1006–1016.

[32] Gutiérrez MA. Energy release control for numerical simulations of failure in quasi-brittle solids. *Communications in Numerical Methods in Engineering* 2004; **20**:19–29.

[33] van der Meer FP, Oliver C, Sluys LJ. Computational analysis of progressive failure in a notched laminate including shear nonlinearity and fiber failure. *Composites Science and Technology* 2010; **70**:692–700.

[34] van der Meer FP. Mesolevel modeling of failure in composite laminates: Constitutive, kinematic and algorithmic aspects. *Archives of Computational Methods in Engineering* 2012; **19**:381–425.

[35] Rocha IBCM, Raijmaekers S, Nijssen RPL, van der Meer FP, Sluys LJ. Experimental/numerical study of anisotropic water diffusion in glass/epoxy composites. *IOP Conference Series: Materials Science and Engineering* 2016; **139**:1–8.

[36] Geuzaine C, Remacle JF. Gmsh: A three-dimensional finite element mesh generator with built-in pre- and post-processing facilities. *International Journal for Numerical Methods in Engineering* 2009; **79**:1309–1331.

[37] Qian C, Westphal T, Nijssen RPL. Micro-mechanical fatigue modelling of unidirectional glass fibre reinforced polymer composites. *Computational Materials Science* 2013; **69**:62–72.

[38] Li M. *Temperature and moisture effects on composite materials for wind turbine blades*. MSc thesis, Montana State University-Bozeman, 2000.

[39] Nguyen VP, Lloberas Valls O, Stroeven M, Sluys LJ. On the existence of representative volumes for softening quasi-brittle materials - a failure zone averaging scheme. *Computer Methods in Applied Mechanics and Engineering* 2010; **199**:45–48.